

Internal mixing of rotating stars inferred from dipole gravity modes

Peer-reviewed author version

Pedersen, MG; AERTS, Conny; Papics, PI; Michielsen, M; Gebruers, S; Rogers, TM; MOLENBERGHS, Geert; Burssens, S; Garcia, S & Bowman, DM (2021) Internal mixing of rotating stars inferred from dipole gravity modes. In: Nature Astronomy, 5 (7) , p. 715 -722.

DOI: 10.1038/s41550-021-01351-x

Handle: <http://hdl.handle.net/1942/36352>

1 Internal mixing of rotating stars inferred from dipole  
2 gravity modes

3 May G. Pedersen<sup>1,2\*</sup>, Conny Aerts<sup>1,3,4</sup>, Péter I. Pápics<sup>1</sup>, Mathias Michielsen<sup>1</sup>,  
Sarah Gebruers<sup>1,4</sup>, Tamara M. Rogers<sup>5,6</sup>, Geert Molenberghs<sup>7,8</sup>,  
Siemen Burssens<sup>1</sup>, Stefano Garcia<sup>1</sup>, Dominic M. Bowman<sup>1</sup>

<sup>1</sup>Institute of Astronomy, KU Leuven, Celestijnenlaan 200D,  
3001 Leuven, Belgium

<sup>2</sup>Kavli Institute for Theoretical Physics, Kohn Hall, University of California,  
Santa Barbara, CA 93106, USA

<sup>3</sup>Department of Astrophysics, IMAPP, Radboud University Nijmegen,  
P. O. Box 9010, 6500 GL Nijmegen, the Netherlands

<sup>4</sup>Max Planck Institute for Astronomy, Koenigstuhl 17, 69117 Heidelberg, Germany

<sup>5</sup>Department of Mathematics, Statistics and Physics, Newcastle University,  
Newcastle upon Tyne, UK

<sup>6</sup>Planetary Science Institute, Tucson, AZ 85721, USA

<sup>7</sup>I-BioStat, Universiteit Hasselt, Martelarenlaan 42, B-3500 Hasselt, Belgium

<sup>8</sup>I-BioStat, KU Leuven, Kapucijnenvoer 35, B-3000 Leuven, Belgium

4 **During most of their life, stars fuse hydrogen into helium in their core. Mixing**  
5 **of chemical elements in the radiative envelope of stars with a convective core**

---

\*mgpedersen@kitp.ucsb.edu

6 is able to replenish it with **extra** fuel. If effective, such deep mixing allows  
7 stars to live longer and change their evolutionary **path**. Yet, internal mixing  
8 remained unconstrained by *in-situ* observations. Gravity modes probe the deep  
9 stellar interior near the convective core and allow to calibrate internal mixing  
10 **processes**. Here we provide core-to-surface mixing profiles inferred from ob-  
11 served dipole gravity modes in 26 rotating stars with masses between 3 and  
12 10 solar masses. We find a wide range of internal mixing levels across the  
13 sample. Stellar models with stratified mixing profiles in the envelope reveal  
14 the best asteroseismic performance. Our results provide observational guid-  
15 ance for 3-dimensional hydrodynamical simulations of transport processes in  
16 the deep interiors of stars.

17

18 Stars more than twice as massive as the Sun perform the hydrogen fusion in their core  
19 via the CNO-cycle, where isotopes of carbon, nitrogen, and oxygen act as catalysts in  
20 the nuclear reactions<sup>1</sup>. The large amount of energy released in the CNO-cycle causes the  
21 cores of these stars to be convective and fully mixed on a dynamical time scale. As a  
22 consequence all the hydrogen that enters the convective core can be used as fuel. For this  
23 reason, any mixing processes occurring in the transition region between the convective  
24 core and the envelope and managing to transport chemical elements into the core have a  
25 major effect on the evolution of all stars born with a convective core<sup>2</sup>.

26 The global distribution of the chemical elements inside a star is determined by numer-  
27 ous dynamical processes, aside from nuclear reactions. The transport of elements caused  
28 by gradients of physical quantities is a diffusive process<sup>3</sup>, while global large-scale displace-  
29 ments, such as circulation due to rotation, happen via advection<sup>4</sup>. Numerous transport  
30 processes with a diversity of efficiencies, interactions, and time scales act together in the  
31 radiative envelope<sup>5–8</sup> and have the potential to inject fresh hydrogen into the convective  
32 core, leading to a more massive helium core as long as the hydrogen fusion continues.  
33 Conversely, material processed by core fusion may be transported to the surface of the  
34 star, where it changes the abundances<sup>9</sup>.

35 The evolution of the mass fraction of a chemical element  $i$  at distance  $r$  from the stellar  
 36 center,  $X_i(r)$ , requires solving a 3-dimensional diffusion-advection transport equation,  
 37 leading to latitudinal variation in the extent of mixing, as well as time-dependent mixing  
 38 profiles<sup>10</sup>. However, in the case of a spherical star with strong horizontal turbulence due  
 39 to dynamical processes, it has been shown that the vertical advection can be treated  
 40 diffusively<sup>11</sup>, which is the approach we adopt here. In this case, the transport equation  
 41 simplifies to

$$\frac{\partial X_i(r)}{\partial t} = \mathcal{R}_i(r) + \frac{1}{\rho(r)r^2} \frac{\partial}{\partial r} \left[ \rho(r)r^2 D_{\text{mix}}(r) \frac{\partial X_i(r)}{\partial r} \right], \quad (1)$$

42 where  $\mathcal{R}_i(r)$  is the local rate of change of  $X_i(r)$  due to nuclear reactions and  $D_{\text{mix}}(r)$  is  
 43 the mixing profile from the core to the surface of the star covering three regions: the  
 44 convective core with mixing coefficient  $D_{\text{conv}}(r)$ , the radiative envelope with coefficient  
 45  $D_{\text{env}}(r)$ , and the core boundary layer, which is the transition zone between the two, with  
 46 mixing coefficient  $D_{\text{cbl}}(r)$ .

47 Extensive theoretical and numerical computations of transport processes for core  
 48 boundary layers<sup>12,13</sup> and stellar envelopes<sup>14,15</sup> have been made and their results included in  
 49 stellar models across a large mass range<sup>4,16</sup>. Surface abundances and model-independent  
 50 dynamical masses of massive eclipsing binaries have been used to evaluate transport pro-  
 51 cesses<sup>9,17-19</sup>. These observational studies reveal that  $D_{\text{mix}}(r)$  is the dominant uncertainty  
 52 in the theory of stellar evolution for the majority of single and binary stars born with  
 53  $M \gtrsim 1.2 M_{\odot}$ .

54 Asteroseismology is a powerful tool making stellar interiors accessible to observational  
 55 probing<sup>20</sup>. It relies on the interpretation of detected oscillation modes, which are sensitive  
 56 to the local conditions in the deep stellar interior. Gravity (g) modes are particularly  
 57 sensitive to the physics of the convective boundary layers and are therefore an excellent  
 58 *in-situ* probe to assess  $D_{\text{cbl}}(r)$ . A key observational diagnostic is the period spacing  
 59 pattern of g modes with the same degree  $\ell$  and azimuthal order  $m$ , but with consecutive  
 60 radial orders  $n$ ,  $\Delta P_{\ell,m,n} \equiv P_{\ell,m,n} - P_{\ell,m,n-1}$ <sup>21</sup>. This diagnostic quantity has been used to  
 61 probe the physics in convective boundary layers of evolved stars and white dwarfs with

62 short-period g modes (periods of minutes to hours) and slow rotation (periods of days)<sup>22</sup>.  
 63 Here, we measure period spacing patterns of 26 slowly pulsating B-type (SPB) stars, whose  
 64 g modes and rotation have similar periods (of the order of a day), with the aim to infer  
 65  $D_{\text{mix}}(r)$  throughout their interior. Their photometric light curves assembled by the *Kepler*  
 66 space telescope<sup>23</sup> shown in Figure 1 (and Supplementary Figures 1 to 26) are subjected to  
 67 Fourier analysis and to the method of iterative prewhitening (see *Methods*) to derive period  
 68 spacing patterns  $\Delta P_{\ell,m,n}$  of dipole modes as in Figure 2 (and Supplementary Figures 1  
 69 to 26). For a chemically homogeneous, non-rotating star the period spacing patterns  
 70 are constant and their values are mainly determined by the mass and age of the star,  
 71 with more massive and younger stars having higher period spacing values. Deviations  
 72 from constant patterns result due to changes in the internal chemical profiles,  $X_i(r)$ ,  
 73 occurring naturally as the star evolves. The patterns are further modified by internal  
 74 mixing processes. The age and internal mixing profile,  $D_{\text{mix}}(r)$ , hence determine the  
 75 overall morphology of the patterns. The rotation of the star induces a slope in its period  
 76 spacing patterns. This slope increases for higher rotation rates and shifts the patterns  
 77 towards shorter periods in the case of prograde modes. Of the six stars in Figure 2,  
 78 KIC 8714886 and KIC 4936089 have the lowest rotation rates and KIC 8714886 is more  
 79 massive than KIC 4936089, which explains why the period spacing values of KIC 8714886  
 80 are higher than those of KIC 4936089. The observed patterns are used to derive an initial  
 81 estimate of the rotational frequency in the core boundary layer,  $\Omega_{\text{rot}}$ , from their slope<sup>24</sup>.  
 82 We find that almost all the detected dipole modes occur in the gravito-inertial regime,  
 83 where the mode frequencies are below twice the rotation frequency. This regime requires  
 84 pulsation computations to be done from a non-perturbative treatment of the Coriolis  
 85 acceleration<sup>25</sup>.

86 Modelling of the dipole period spacings is performed using a grid-based statistical  
 87 approach allowing for uncertainty in the theoretical period spacing predictions due to im-  
 88 perfect input physics of the equilibrium models. We consider eight grids of non-rotating  
 89 1-D equilibrium models and compute their oscillation modes in the presence of the Corio-  
 90 lis acceleration<sup>26</sup>. The stellar models are represented by a set of fixed input physics  $\psi$  (see

91 *Methods*) and a number of free parameters  $\theta$  discussed below. Each grid covers the entire  
 92 phase of hydrogen fusion in the core, the mass range  $M_{\text{ini}} \in [2.75, 10.0] M_{\odot}$  and initial  
 93 metallicity  $Z \in [0.003, 0.04]$ , but having a different mixing profile in the core boundary  
 94 layer  $D_{\text{cbl}}(r)$  and in the envelope  $D_{\text{env}}(r)$ . Each of these two profiles has one free param-  
 95 eter:  $\alpha_{\text{cbl}}$  and  $D_{\text{env},0}$ , respectively. Here,  $\alpha_{\text{cbl}}$  is a length scale connected with the size of  
 96 the core boundary layer, while  $D_{\text{env},0}$  represents the level of mixing at the bottom of the  
 97 radiative envelope (see *Methods*). For  $D_{\text{cbl}}(r)$  the profile due to either convective penetra-  
 98 tion<sup>12</sup> or diffusive exponential overshooting<sup>27</sup> is adopted. For the envelope, a multitude of  
 99 mixing profiles caused by various physical phenomena occurs in the literature. Here, we  
 100 utilise four typical profiles,  $D_{\text{env}}(r)$ : constant, wave mixing<sup>28</sup>, mixing due to vertical shear  
 101 resulting from instabilities<sup>29</sup>, or meridional circulation combined with large horizontal and  
 102 vertical shear<sup>4</sup>, all of which the effect of mixing can be described diffusively. The result-  
 103 ing eight different  $D_{\text{mix}}(r)$  are illustrated in Figure 3 and represented by  $\psi_1, \dots, \psi_8$  as  
 104 indicated in each of the subpanels of the figure. For each of these eight grids we compute  
 105 statistical models which predict the theoretical period spacing values as a function of the  
 106 components of  $\theta$ , allowing us to refine the grid resolution between each of the grid points  
 107 without having to compute additional stellar models and their oscillation properties (see  
 108 *Methods*). With our approach, we provide an asteroseismic evaluation of mixing based on  
 109 a sample of g-mode pulsators treated in a homogeneous way, rather than just treating one  
 110 star at a time as done so far<sup>30</sup>. Since the mixing profiles are expected to change during  
 111 the evolution but it is unknown in what way<sup>10</sup>, we evaluate whether  $\alpha_{\text{cbl}}$  or  $D_{\text{env},0}$  are  
 112 associated with the evolutionary stage of the SPB stars in our sample.

113 Asteroseismic modelling of the 26 SPB stars based on their gravito-inertial dipole  
 114 period spacings (cf. Figure 2 and Supplementary Figures 1 to 26), delimiting the permitted  
 115 parameter space to that denoted by the spectroscopic and astrometric constraints for each  
 116 star, is done by maximum likelihood estimation of the six free parameters upon which  
 117 each of the eight model grids are built (see *Methods*). This leads to each star’s mass,  
 118 metal mass fraction, evolutionary status, interior rotation frequency, convective boundary  
 119 mixing, and mixing at the bottom of the envelope, represented by the parameter vector

120  $\theta \equiv (M_{\text{ini}}, Z, X_c/X_{\text{ini}}, \Omega_{\text{rot}}, \alpha_{\text{cbl}}, D_{\text{env},0})$ . Here,  $X_c$  is the fractional mass of hydrogen left  
121 in the fully mixed convective core and is a proxy for the stellar age, while  $X_{\text{ini}}$  is the initial  
122 hydrogen mass fraction. Figure 2 and Supplementary Figures 1 to 26 show the theoretical  
123 period spacings for the grid that best represents this measured diagnostic for each of the  
124 26 SPB stars (the accompanying  $\theta$  is listed in Supplementary Table 1). So far, only  
125 two of these SPBs were asteroseismically modelled with non-perturbative inclusion of the  
126 Coriolis acceleration; in both cases a constant level of envelope mixing was enforced and  
127 precision estimation of  $\theta$  was not considered<sup>30,31</sup>. We assess the 6-D uncertainty regions  
128 of  $\theta$  from a Monte Carlo approach (see *Methods*) and compute a weighted average for the  
129 stellar mass, evolutionary stage, metallicity and rotation frequency across the eight grids  
130 (Supplementary Table 2).

131 Each of our stars' dominant frequency extends the range of this observable obtained  
132 previously for 13 high-amplitude SPB stars studied from ground-based data<sup>32</sup> (see Sup-  
133plementary Figures 27 and 28 and Supplementary Information). To quantify whether  
134 these dominant frequencies and their amplitudes correlate with the effective temperature,  
135 surface gravity, luminosity, and stellar mass, we calculate Spearman's rank correlation  
136 coefficients  $r_s$ , which take values between  $-1$  and  $+1$ , where  $r_s = +1$  indicates a perfect  
137 positive correlation,  $r_s = -1$  a perfect negative correlation, and  $r_s = 0$  uncorrelated data.  
138 The  $r_s$  values are listed in Supplementary Table 3 for the cases where the  $p$ -values are  
139  $< 0.05$ , implying that we can reject the null-hypothesis of them being equal to zero at  
140 the 95% confidence level. We find that the amplitudes of the dominant modes are neg-  
141 atively correlated with the mass, effective temperature, and luminosity of the star and  
142 positively correlated with the surface gravity for the 26 SPB stars. Our sample covers  
143 the entire SPB instability strip<sup>33</sup> and rotation rates from almost zero up to almost the  
144 critical rotation rate, i.e.,  $\Omega_{\text{rot}}/\Omega_{\text{crit}} \in [0, 1]$ . The asteroseismic results reveal Gaia DR2  
145 luminosities and spectroscopic masses of B stars to be underestimated, which is a result  
146 of the lower effective temperature estimates from the Gaia DR2 data<sup>34,35</sup> (Supplementary  
147 Information, Supplementary Figure 30 and Table 5).

148 None of the mixing profiles provides the best solution for all 26 SPB stars, i.e., diversity

149 occurs in the internal mixing **properties, with a wide variety of mixing efficiencies**. We find  
 150 that the majority of stars, i.e., 17 of the 26 SPB stars, are best modelled via convective  
 151 penetration in the core boundary layer, while diffusive core overshooting offers a better  
 152 explanation for the other nine. Eleven SPB stars reveal the best match for the envelope  
 153 mixing profile based on vertical shear mixing, while seven stars are best modelled with a  
 154 gravity-wave mixing profile, five with a constant profile, and four with a profile combining  
 155 meridional circulation with vertical shear (cf. Figure 4 **and Supplementary Information**).  
 156 Figure 5 visualizes the inferred mixing profiles of the optimal solutions found for all 26  
 157 SPB stars as listed in Supplementary Table 1 and reveals a wide range of mixing levels  
 158 across the evolution, with  $D_{\text{env},0} \in [12, 8.7 \times 10^5] \text{ cm}^2 \text{ s}^{-1}$ . **We find that nine out of 26**  
 159 **SPB stars rotate above 70% of their critical break-up velocity, which implies that future**  
 160 **modelling based on 2-D stellar evolution models should be attempted whenever proper**  
 161 **tools become available.**

162 Figure 6 shows correlations among estimated parameters and two inferred quantities  
 163 of importance for the further evolution of the stars resulting from  $\theta$ , i.e., the fractional  
 164 Schwarzschild convective core mass and size,  $m_{\text{cc}}/M$  and  $r_{\text{cc}}/R$ . **Despite several large**  
 165 **and asymmetrical uncertainty intervals resulting from projections of the 6-D elongated**  
 166 **uncertainty regions onto 1-D**, we find that both of these quantities decrease as the evolu-  
 167 tion progresses, as expected from theory<sup>36</sup> and from hydrodynamical simulations<sup>10</sup>. The  
 168 g modes allow for proper inference of the core masses despite considerable uncertainty  
 169 for  $\alpha_{\text{cbl}}$  in the 6-D fitting. The convective core mass expressed as a percentage of total  
 170 stellar mass ranges from  $\sim 30\%$  near the zero-age-main-sequence (ZAMS) and stays above  
 171  $\sim 6\%$  near the terminal-age-main-sequence (TAMS), confirming the need for higher-than-  
 172 standard core masses in eclipsing binaries<sup>19</sup> and in young open clusters<sup>37,38</sup>. Through the  
 173 calculation of Spearman’s rank correlation coefficients (Supplementary Table 7) we find a  
 174 strong correlation between  $r_{\text{cc}}/R$  and  $m_{\text{cc}}/M$  as well as between the core masses and radii  
 175 and the main-sequence evolutionary stage  $X_c/X_{\text{ini}}$ , as expected from theory. The convec-  
 176 tive core size is uncorrelated to the level of envelope mixing, while the convective core  
 177 mass correlates **moderately with it, as shown in Figure 6** for values  $D_{\text{env},0} \gtrsim 10^3 \text{ cm}^2 \text{ s}^{-1}$ .

178 This points to envelope material getting efficiently transported to the core for such levels  
179 of mixing.

180 Aside from **the slow rotator** KIC 8459899, whose asteroseismic modelling led to low  
181 metallicity,  $D_{\text{env},0}$  increases with increasing  $\Omega_{\text{rot}}/\Omega_{\text{crit}}$  irrespective of the mass and evolu-  
182 tionary stage. Higher  $D_{\text{env},0}$  values lead to higher core masses (Supplementary Table 7),  
183 while no correlation is found between  $D_{\text{env},0}$  and  $X_{\text{c}}/X_{\text{ini}}$  at the 95% confidence level. For  
184 KIC 3240411, similar results **to ours** were achieved from modelling based on 1-D equilib-  
185 rium models **with rotational mixing**<sup>31</sup>. We added published results for two slowly rotating  
186 SPB stars in Figure 6. These were modelled using the same input physics as in our  $\psi_1$ <sup>39,40</sup>,  
187 but by adopting a perturbative treatment for the Coriolis acceleration rather than the  
188 TAR as in the current work. For reasons of consistency, these two stars were not included  
189 in our computations of the Spearman’s rank correlation coefficients listed in Supplemen-  
190 tary Table 7. Figure 6 shows that the three slowest rotators, where two are metal-poor  
191 and one is metal-rich, reveal considerable levels of envelope mixing. We find no other  
192 clear correlations between the remaining estimated  $\theta$  values and hence do not provide the  
193 correlation coefficients for them.

194 Our homogeneous analysis based on a sample of g-mode pulsators **offers the oppor-**  
195 **tunity to evaluate the quality of the input physics of stellar models in the covered mass**  
196 **and age range. We conclude that the internal mixing profiles of almost all SPB stars as**  
197 **inferred from asteroseismology are radially stratified instead of constant.** Future deriva-  
198 tion of rotation and mixing profiles,  $\Omega(r, t)$  and  $D_{\text{mix}}(r, t)$ , without having to rely on  
199 predefined time-independent profiles as done so far, can be achieved from a much larger  
200 sample of SPB stars with sufficient identified g modes having proper probing capacity.  
201 Such observationally calibrated mixing profiles and the resulting helium core masses near  
202 core hydrogen exhaustion constitute important asteroseismic input to improve stellar evo-  
203 lution models and chemical yield computations for the evolved stages of stars born with  
204 a mass above three solar masses.

## References

- [1] Nomoto, K., Kobayashi, C., and Tominaga, N., Nucleosynthesis in Stars and the Chemical Enrichment of Galaxies, *Ann. Rev. Astron. Astrophys.*, **51**, 457–509, (2013).
- [2] Maeder, A. and Meynet, G., The Evolution of Rotating Stars, *Ann. Rev. Astron. Astrophys.*, **38**, 143–190, (2000).
- [3] Salaris, M. and Cassisi, S., Chemical element transport in stellar evolution models, *Royal Society Open Science*, **4**, 170192, (2017).
- [4] Georgy, C., *et al.*, Populations of rotating stars. I. Models from 1.7 to 15  $M_{\odot}$  at  $Z = 0.014$ , 0.006, and 0.002 with  $\Omega/\Omega_{crit}$  between 0 and 1, *Astron. Astrophys.*, **553**, A24, (2013).
- [5] Zahn, J. P., Circulation and turbulence in rotating stars., *Astron. Astrophys.*, **265**, 115–132, (1992).
- [6] Chaboyer, B., Demarque, P., and Pinsonneault, M. H., Stellar Models with Microscopic Diffusion and Rotational Mixing. I. Application to the Sun, *Astrophys. J.*, **441**, 865, 1995.
- [7] Mathis, S. and Zahn, J. P., Transport and mixing in the radiation zones of rotating stars. II. Axisymmetric magnetic field, *Astron. Astrophys.*, **440**, 653–666, (2005).
- [8] Rogers, T. M., Lin, D. N. C., McElwaine, J. N., and Lau, H. H. B., Internal Gravity Waves in Massive Stars: Angular Momentum Transport, *Astrophys. J.*, **772**, 21, (2013).
- [9] Brott, I., *et al.*, Rotating massive main-sequence stars. I. Grids of evolutionary models and isochrones, *Astron. Astrophys.*, **530**, A115, (2011).
- [10] Deupree, R. G., Stellar Evolution with Arbitrary Rotation Laws. III. Convective Core Overshoot and Angular Momentum Distribution, *Astrophys. J.*, **499**, 340–347, (1998).

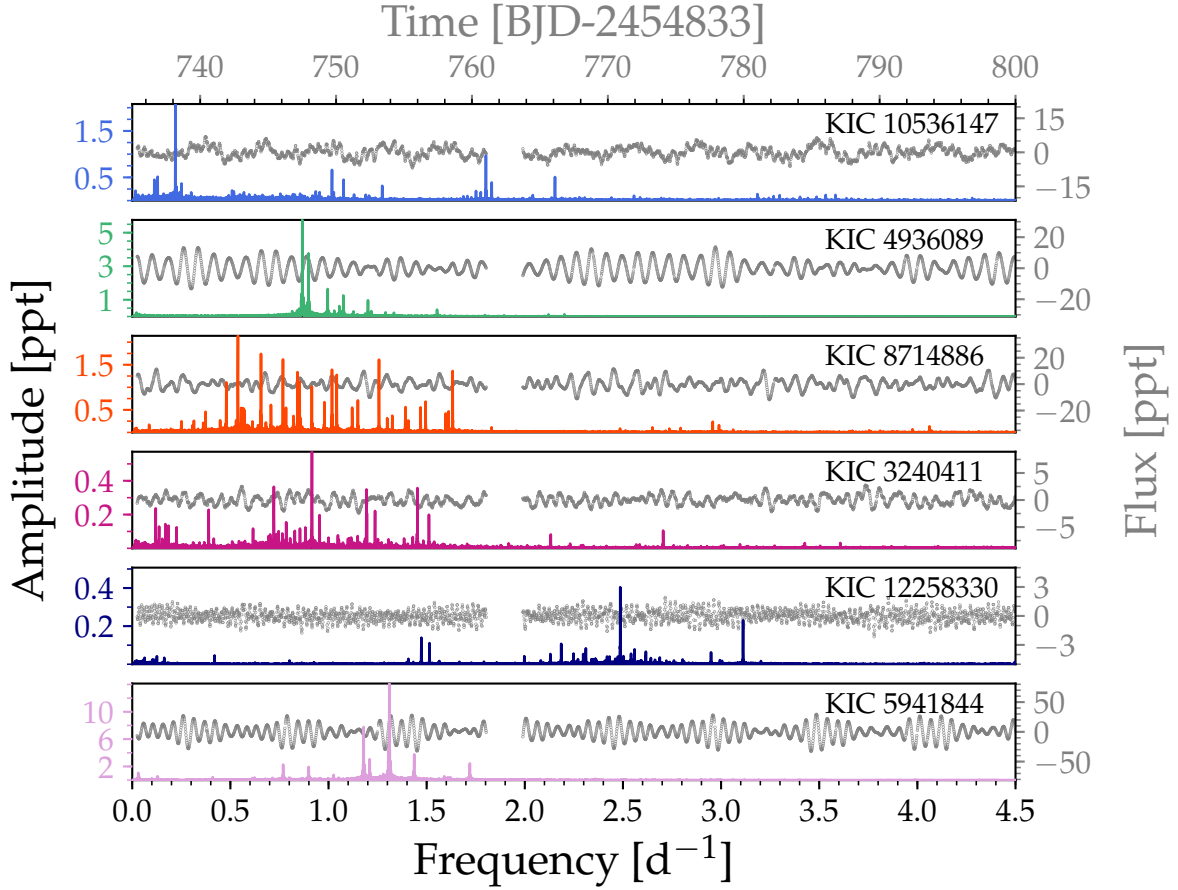
- 231 [11] Chaboyer, B. and Zahn, J. P., Effect of horizontal turbulent diffusion on transport  
232 by meridional circulation., *Astron. Astrophys.*, **253**, 173–177, (1992).
- 233 [12] Zahn, J. P., Convective penetration in stellar interiors., *Astron. Astrophys.*, **252**,  
234 179–188, (1991).
- 235 [13] Freytag, B., Ludwig, H.-G., and Steffen, M., Hydrodynamical models of stellar con-  
236 vection. The role of overshoot in DA white dwarfs, A-type stars, and the Sun., *Astron.*  
237 *Astrophys.*, **313**, 497–516, (1996).
- 238 [14] Pinsonneault, M., Mixing in Stars, *Ann. Rev. Astron. Astrophys.*, **35**, 557–605,  
239 (1997).
- 240 [15] Charbonnel, C. and Lagarde, N., Thermohaline instability and rotation-induced mix-  
241 ing. I. Low- and intermediate-mass solar metallicity stars up to the end of the AGB,  
242 *Astron. Astrophys.*, **522**, A10, (2010).
- 243 [16] Dotter, A., *et al.*, The Dartmouth Stellar Evolution Database, *Astrophys. J. Suppl.*  
244 *Ser.*, **178**, 89–101, (2008).
- 245 [17] Morel, T., Hubrig, S., and Briquet, M., Nitrogen enrichment, boron depletion and  
246 magnetic fields in slowly-rotating B-type dwarfs, *Astron. Astrophys.*, **481**, 453–463,  
247 (2008).
- 248 [18] Martins, F., *et al.*, Observational effects of magnetism in O stars: surface nitrogen  
249 abundances, *Astron. Astrophys.*, **538**, A29, (2012).
- 250 [19] Tkachenko, A., *et al.*, The mass discrepancy in intermediate- and high-mass eclipsing  
251 binaries: The need for higher convective core masses, *Astron. Astrophys.*, **637**, A60,  
252 (2020).
- 253 [20] Aerts, C., Christensen-Dalsgaard, J., and Kurtz, D. W., *Asteroseismology*, *Astron-*  
254 *omy and Astrophysics Library*, Springer Berlin Heidelberg. (2010).

- 255 [21] Miglio, A., Montalbán, J., Noels, A., and Eggenberger, P., Probing the properties of  
256 convective cores through g modes: high-order g modes in SPB and  $\gamma$  Doradus stars,  
257 *Mon. Not. R. Astron. Soc.*, **386**, 1487–1502, (2008).
- 258 [22] Bossini, D., *et al.*, Uncertainties on near-core mixing in red-clump stars: effects on  
259 the period spacing and on the luminosity of the AGB bump, *Mon. Not. R. Astron.*  
260 *Soc.*, **453**, 2290–2301, (2015).
- 261 [23] Koch, D. G., *et al.*, Kepler Mission Design, Realized Photometric Performance, and  
262 Early Science, *Astrophys. J. Lett.*, **713**, L79–L86, (2010).
- 263 [24] Van Reeth, T., Tkachenko, A., and Aerts, C., Interior rotation of a sample of  $\gamma$  Do-  
264 radus stars from ensemble modelling of their gravity-mode period spacings, *Astron.*  
265 *Astrophys.*, **593**, A120, (2016).
- 266 [25] Bouabid, M. P., *et al.*, Effects of the Coriolis force on high-order g modes in  $\gamma$  Doradus  
267 stars, *Mon. Not. R. Astron. Soc.*, **429**, 2500–2514, (2013).
- 268 [26] Aerts, C., *et al.*, Forward Asteroseismic Modeling of Stars with a Convective Core  
269 from Gravity-mode Oscillations: Parameter Estimation and Stellar Model Selection,  
270 *Astrophys. J. Suppl. Ser.*, **237**, 15, (2018).
- 271 [27] Herwig, F., The evolution of AGB stars with convective overshoot, *Astron. Astro-*  
272 *phys.*, **360**, 952–968, (2000).
- 273 [28] Rogers, T. M. and McElwaine, J. N., On the Chemical Mixing Induced by Internal  
274 Gravity Waves, *Astrophys. J. Lett.*, **848**, L1, (2017).
- 275 [29] Mathis, S., Palacios, A., and Zahn, J. P., On shear-induced turbulence in rotating  
276 stars, *Astron. Astrophys.*, **425**, 243–247, (2004).
- 277 [30] Moravveji, E., Townsend, R. H. D., Aerts, C., and Mathis, S., Sub-inertial Gravity  
278 Modes in the B8V Star KIC 7760680 Reveal Moderate Core Overshooting and Low  
279 Vertical Diffusive Mixing, *Astrophys. J.*, **823**, 130, (2016).

- 280 [31] Szewczuk, W. and Daszyńska-Daszkiewicz, J., KIC 3240411 - the hottest known SPB  
281 star with the asymptotic g-mode period spacing, *Mon. Not. Roy. Astron. Soc.*, **478**,  
282 2243–2256, (2018).
- 283 [32] De Cat, P. and Aerts, C., A study of bright southern slowly pulsating B stars. II.  
284 The intrinsic frequencies, *Astron. Astrophys.*, **393**, 965–981, (2002).
- 285 [33] Szewczuk, W. and Daszyńska-Daszkiewicz, J., Domains of pulsational instability of  
286 low-frequency modes in rotating upper main sequence stars, *Mon. Not. R. Astron.*  
287 *Soc.*, **469**, 13–46, (2017).
- 288 [34] Anders, F., *et al.*, Photo-astrometric distances, extinctions, and astrophysical pa-  
289 rameters for Gaia DR2 stars brighter than  $G = 18$ , *Astron. Astrophys.*, **628**, A94,  
290 (2019).
- 291 [35] Pedersen, M. G., Escorza, A., Pápics, P. I., and Aerts, C., Recipes for bolometric  
292 corrections and Gaia luminosities of B-type stars: application to an asteroseismic  
293 sample, *Mon. Not. R. Astron. Soc.*, **495**, 2738–2753, (2020).
- 294 [36] Kippenhahn, R., Weigert, A., and Weiss, A., *Stellar Structure and Evolution*, *As-*  
295 *tronomy and Astrophysics Library*, Springer Berlin Heidelberg. (2012).
- 296 [37] Li, C., *et al.*, Extended Main-sequence Turnoffs in the Double Cluster h and  $\chi$  Persei:  
297 The Complex Role of Stellar Rotation, *Astrophys. J.*, **876**, 65, (2019).
- 298 [38] Johnston, C., Aerts, C., Pedersen, M. G., and Bastian, N., Isochrone-cloud fitting  
299 of the extended main-sequence turn-off of young clusters, *Astron. Astrophys.*, **632**,  
300 A74, (2019).
- 301 [39] Wu, T., *et al.*, Asteroseismic Analyses of Slowly Pulsating B Star KIC 8324482:  
302 Ultraweak Element Mixing beyond the Central Convective Core, *Astrophys. J.*, **899**,  
303 38, (2020).
- 304 [40] Wu, T. and Li, Y., High-precision Asteroseismology in a Slowly Pulsating B Star:  
305 HD 50230, *Astrophys. J.*, **881**, 86, (2019).

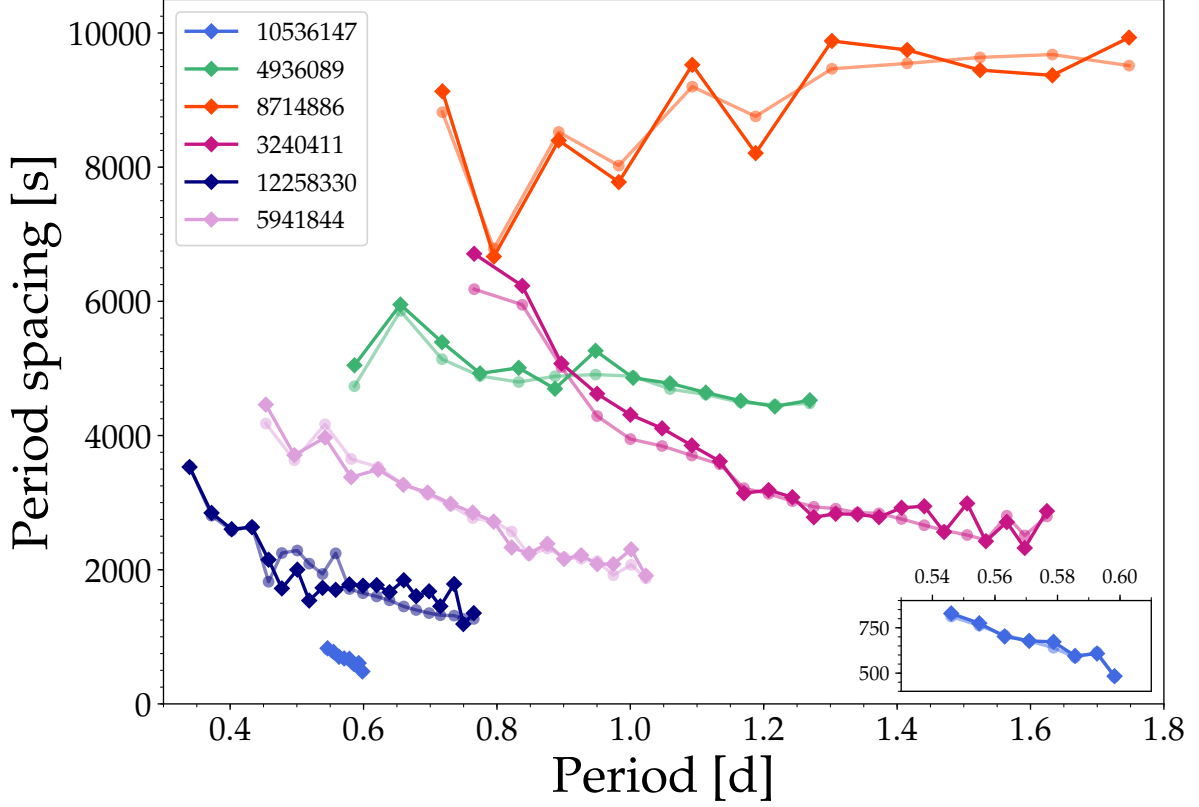
- 306 [41] Balona, L. A., Baran, A. S., Daszyńska-Daszkiewicz, J., and De Cat, P., Analysis  
307 of Kepler B stars: rotational modulation and Maia variables, *Mon. Not. R. Astron.*  
308 *Soc.*, **451**, 1445–1459, (2015).
- 309 [42] Pápics, P. I., *et al.*, Signatures of internal rotation discovered in the Kepler data of  
310 five slowly pulsating B stars, *Astron. Astrophys.*, **598**, A74, (2017).
- 311 [43] Moravveji, E., Aerts, C., Pápics, P. I., Triana, S. A., and Vandoren, B., Tight aster-  
312 oseismic constraints on core overshooting and diffusive mixing in the slowly rotating  
313 pulsating B8.3V star KIC 10526294, *Astron. Astrophys.*, **580**, A27, (2015).
- 314 [44] Triana, S. A., *et al.*, The Internal Rotation Profile of the B-type Star KIC 10526294  
315 from Frequency Inversion of its Dipole Gravity Modes, *Astrophys. J.*, **810**, 16, (2015).
- 316 [45] Aerts, C., Probing the interior physics of stars through asteroseismology, *Rev. of*  
317 *Mod. Phys.*, **93**, 015001, [arXiv:1912.12300](https://arxiv.org/abs/1912.12300), (2021).
- 318 [46] Raskin, G., *et al.*, HERMES: a high-resolution fibre-fed spectrograph for the Mercator  
319 telescope, *Astron. Astrophys.*, **526**, A69, (2011).
- 320 [47] Pápics, P. I., *et al.*, Two new SB2 binaries with main sequence B-type pulsators in  
321 the Kepler field, *Astron. Astrophys.*, **553**, A127, (2013).
- 322 [48] Tkachenko, A., Grid search in stellar parameters: a software for spectrum analysis  
323 of single stars and binary systems, *Astron. Astrophys.*, **581**, A129, (2015).
- 324 [49] Aerts, C., Molenberghs, G., Kenward, M. G., and Neiner, C., The Surface Nitrogen  
325 Abundance of a Massive Star in Relation to its Oscillations, Rotation, and Magnetic  
326 Field, *Astrophys. J.*, **781**, 88, (2014).
- 327 [50] Paxton, B., *et al.*, Modules for Experiments in Stellar Astrophysics (MESA): Pul-  
328 sating Variable Stars, Rotation, Convective Boundaries, and Energy Conservation,  
329 *Astrophys. J. Suppl. Ser.*, **243**, 10, (2019).
- 330 [51] Aerts, C., Mathis, S., and Rogers, T. M., Angular Momentum Transport in Stellar  
331 Interiors, *Annu. Rev. Astron. Astrophys.*, **57**, 35–78, (2019).

- 332 [52] Seaton, M. J., Opacity Project data on CD for mean opacities and radiative acceler-  
333 ations, *Mon. Not. R. Astron. Soc.*, **362**, L1–L3, (2005).
- 334 [53] Przybilla, N., Nieva, M. F., Irrgang, A., and Butler, K., Hot stars and cosmic abun-  
335 dances, in *EAS Publications Series* (Alecian, G., Lebreton, Y., Richard, O., and  
336 Vauclair, G., eds.), 63 of *EAS Publications Series*, 13–23, (2013).
- 337 [54] Vink, J. S., de Koter, A., and Lamers, H. J. G. L. M., Mass-loss predictions for O  
338 and B stars as a function of metallicity, *Astron. Astrophys.*, **369**, 574–588, (2001).
- 339 [55] Björklund, R., Sundqvist, J. O., Puls, J., and Najarro, F., New predictions for  
340 radiation-driven, steady-state mass-loss and wind-momentum from hot, massive stars  
341 II. A grid of O-type stars in the Galaxy and the Magellanic Clouds, *Astron. Astro-*  
342 *phys.*, *in press*, arXiv:2008.06066, (2020).
- 343 [56] Böhm-Vitense, E., Über die Wasserstoffkonvektionszone in Sternen verschiedener  
344 Effektivtemperaturen und Leuchtkräfte. Mit 5 Textabbildungen, *Zeitung für Astro-*  
345 *physik*, **46**, 108, (1958).
- 346 [57] Ouazzani, R.-M., *et al.*, A new asteroseismic diagnostic for internal rotation in  $\gamma$   
347 Doradus stars, *Mon. Not. R. Astron. Soc.*, **465**, 2294–2309, (2017).
- 348 [58] Townsend, R. H. D., Goldstein, J., and Zweibel, E. G., Angular momentum transport  
349 by heat-driven g-modes in slowly pulsating B stars, *Mon. Not. R. Astron. Soc.*, **475**,  
350 879–893, (2018).
- 351 [59] Bellinger, E. P., *et al.*, Fundamental Parameters of Main-Sequence Stars in an Instant  
352 with Machine Learning, *Astrophys. J.*, **830**, 31, (2016).
- 353 [60] Claeskens, G. and Hjort, N. L., *Model Selection and Model Averaging*, *Cambridge*  
354 *Series in Statistical and Probabilistic Mathematics*. (2008).



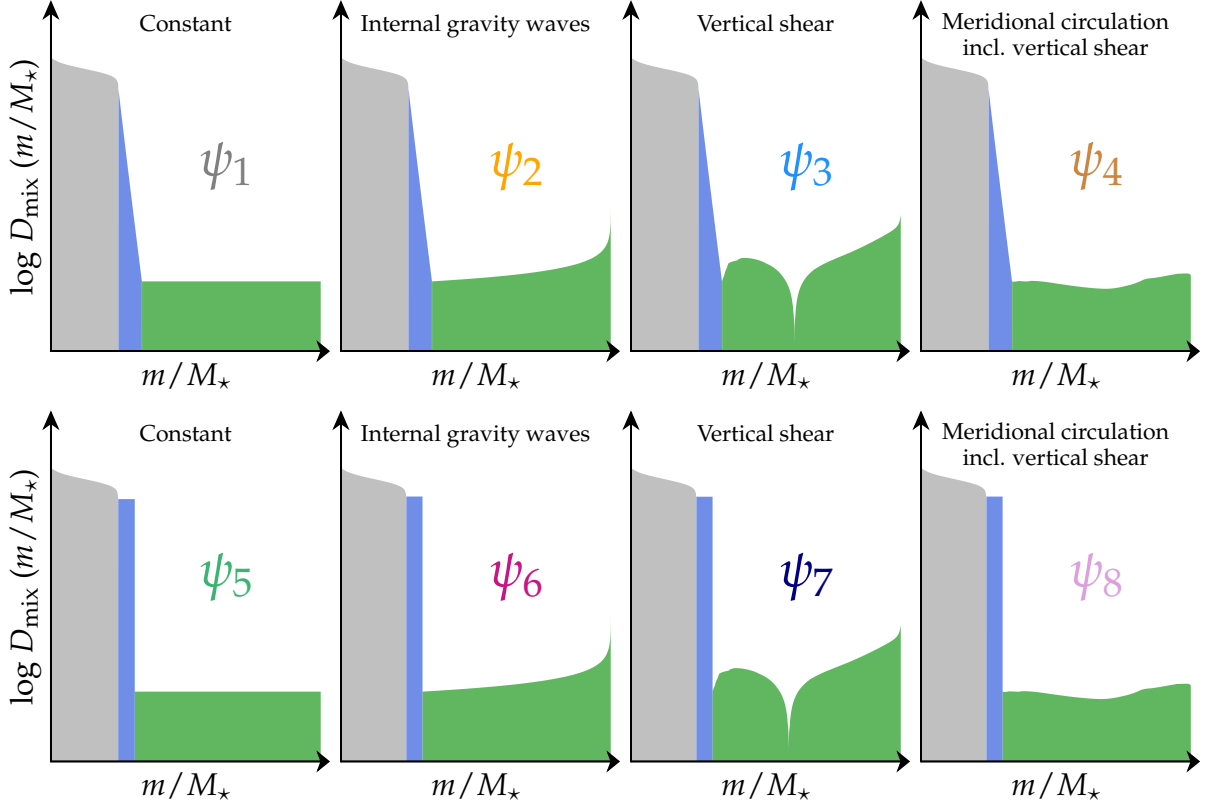
355

356 **Figure 1: Light curves overplotted with amplitude spectra of six Slowly Pul-**  
 357 **sating B stars.** Excerpts from *Kepler* long-cadence ( $\sim 30$  minutes per point) light curves  
 358 (flux as a function of time in grey dots) of six new SPB stars whose *Kepler* Input Cata-  
 359 logue (KIC) identification is indicated. The oscillation spectra (amplitude as a function  
 360 of frequency, coloured lines) derived from the full light curves with a total duration of  
 361  $\sim 1500$  days are overplotted and reveal multiple gravity-mode frequencies with periods of  
 362 the order of days.



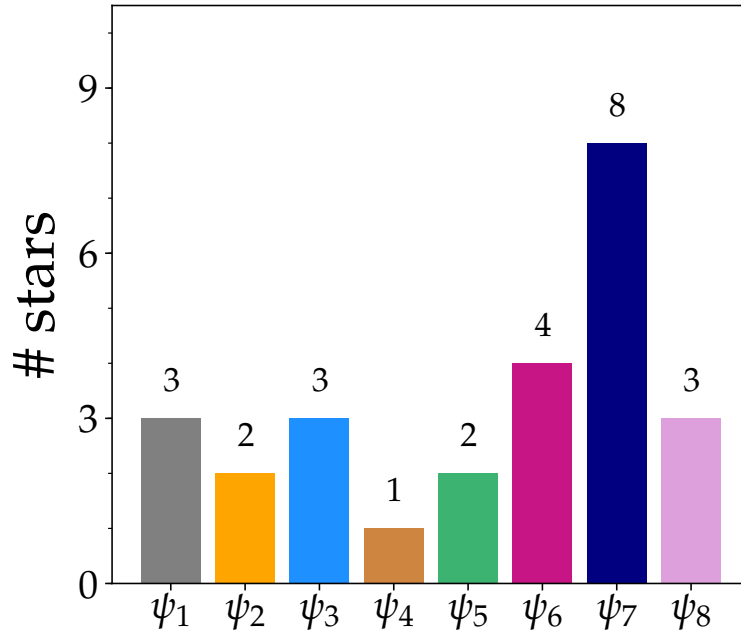
363

364 **Figure 2: Gravity-mode period spacing patterns of six Slowly Pulsating B**  
 365 **stars.** Observed dipole-mode period spacings,  $\Delta P_{1,m,n}$  (indicated in coloured diamonds)  
 366 of the six SPB stars whose light curves and amplitude spectra are shown in Figure 1 are  
 367 compared with the theoretically predicted values (bullets in the same colour with lighter  
 368 colour tone) based on the best stellar evolution model from eight model grids. The formal  
 369 errors of the observed values are smaller than the plotted symbol size for most of the  
 370 detected modes (see *Methods*). The inset contains a zoom in on the SPB with the lowest  
 371 period spacings in the sample. The slope of the patterns correlates with the near-core  
 372 rotation rate. Younger stars and stars of higher mass result in higher period spacing  
 373 values, while the pattern morphology is mainly determined by the evolutionary stage and  
 374 internal mixing.



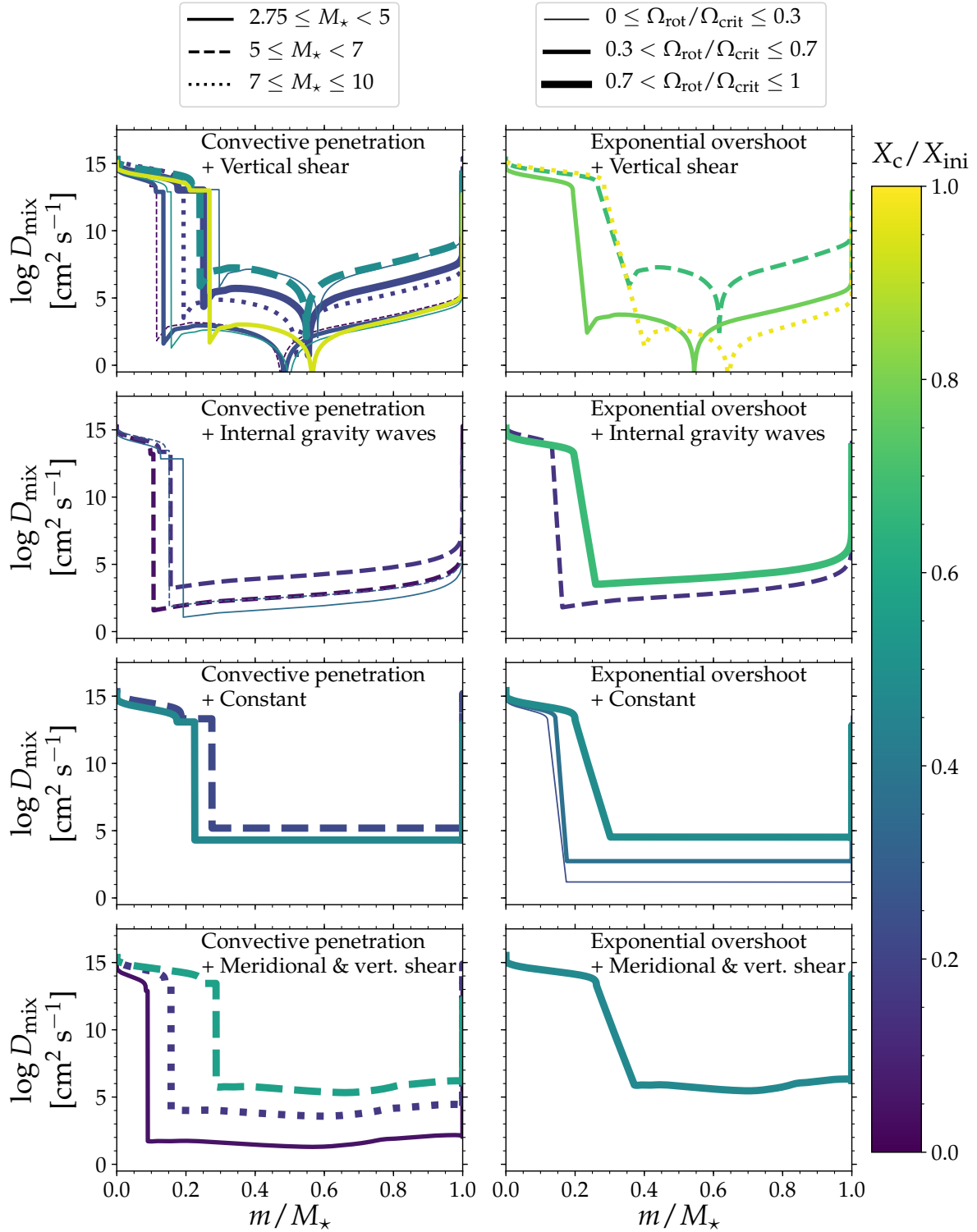
375

376 **Figure 3: Schematic representation of the considered mixing profiles.** The con-  
 377 vective core, convective boundary, and envelope mixing levels as a function of fractional  
 378 mass inside the stellar models are indicated in grey, blue, and green, respectively. Upper  
 379 panels: diffusive exponentially decaying overshooting<sup>27</sup>, lower panels: convective penetra-  
 380 tion<sup>12</sup>. From left to right: constant envelope mixing, mixing caused by internal gravity  
 381 waves<sup>28</sup>, mixing due to vertical shear connected with instabilities<sup>29</sup>, and due to meridional  
 382 circulation caused by rotation combined with vertical shear<sup>4</sup>.



383

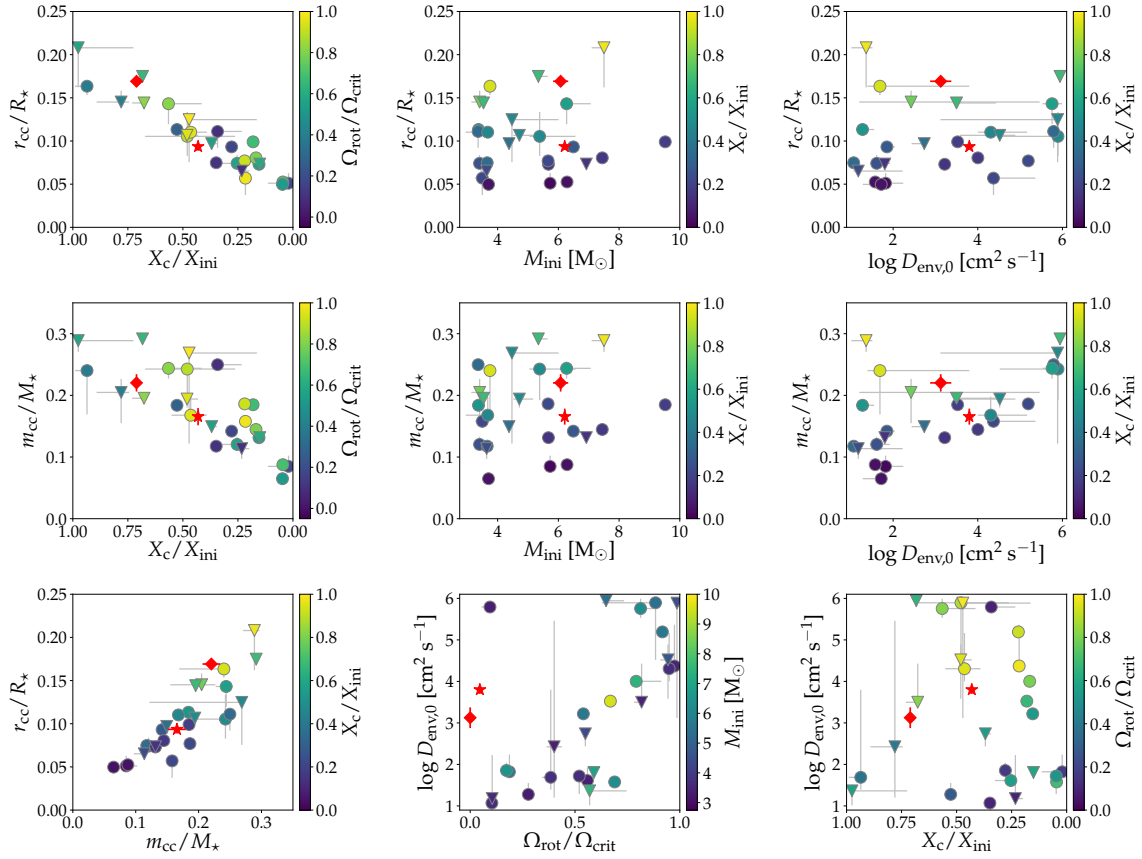
384 **Figure 4: Population of the eight model grids in terms of model capacity.** The  
385 26 SPB stars are distributed over the eight stellar evolution model grids according to the  
386 best solution. The colour of the bars corresponds to the colour of the symbols in Figure 3.



387

388 **Figure 5: Inferred internal mixing profiles for 26 Slowly Pulsating B stars.**

389 The results from the asteroseismic modelling based on the detected gravito-inertial dipole  
 390 modes are overplotted for the 26 best fitting models. The individual profiles are colour  
 391 coded according to their main-sequence evolutionary stage  $X_c/X_{\text{ini}}$ , while the linestyle  
 392 and thickness are related to the mass and rotation rate, respectively.



393

394 **Figure 6: Correlations among estimated parameters and inferred quantities**  
 395 **for the sample.** Stars best modelled by diffusive exponential overshooting in the core  
 396 boundary layer are indicated with triangles, while those best fit by convective penetration  
 397 are shown as circles. Projections of the 6-D uncertainty regions in 1-D for the correspond-  
 398 ing parameter are indicated in grey. We also show published results for the two slowly  
 399 rotating SPB stars KIC 8324482<sup>39</sup> (red diamond) and HD 50230<sup>40</sup> (red star), which have  
 400 been modelled by relying on similar input physics as in our grid  $\psi_1$ , but by adopting a  
 401 perturbative treatment of the Coriolis acceleration rather than the TAR for the pulsation  
 402 computations.

## 403 **Methods**

### 404 **Sample selection, period spacing patterns, and modelling strat-** 405 **egy**

406 We selected 60 candidate Slowly Pulsating B (SPB) stars from various published *Kepler*  
407 variability catalogues, having long cadence (30-min) light curves of 4-year duration from  
408 the nominal *Kepler* mission<sup>23</sup> and revealing at least three independent frequencies in the  
409 g-mode regime. This is half of the discovered SPB stars from the nominal mission and  
410 about 9% of the monitored B-type stars<sup>41</sup>. This restriction of excluding mono- and biperi-  
411 odic g-mode pulsators was built in since our aim is to perform asteroseismic modelling  
412 based on multiple modes whose degree can be identified from period spacing patterns.  
413 We transformed the raw *Kepler* pixel data of all the quarters for these 60 SPB candidates  
414 into light curves using star-dependent customized pixel masks. The merged (over all 18  
415 quarters) and detrended light curves were subjected to frequency analysis by iterative  
416 prewhitening<sup>20</sup>. We retained frequencies with an amplitude above four times the local  
417 noise level computed over a frequency range of  $1 \text{ d}^{-1}$  centred around the considered fre-  
418 quency. Furthermore, we rejected frequencies that are within  $2.5/T$  of one another, where  
419  $T$  is the total length of the time series, and keep only the frequency with the highest am-  
420 plitude within this interval. Among all the remaining significant frequencies, harmonics  
421 and combination frequencies were identified, taking into account the frequency resolution  
422 of the 4-year time series, and excluded for the asteroseismic modelling. Further, we re-  
423 tained only those frequencies with amplitudes significant at  $1\sigma$  level from linear regression  
424 performed in the time domain at each stage of the prewhitening, as an acceptable pro-  
425 cedure to find period spacing patterns of maximal extent in consecutive radial order to  
426 perform the asteroseismic modelling. This led to lists ranging from 37 to 109 independent  
427 mode frequencies to work with for each of the 26 stars. Period spacing patterns were  
428 then searched for among these remaining independent frequencies<sup>42</sup>. In the cases that a  
429 combination frequency fits into the pattern, it was included as part of the pattern as a  
430 combination may occur by chance. We identified period spacing patterns for 26 out of the

431 60 stars. Overall, this implies that  $\sim 4\%$  of all the B stars in the nominal *Kepler* field of  
432 view revealed g-mode pulsations suitable for asteroseismic modelling.

433 Excerpts of the light curves, Fourier transforms of the full 4-year light curves, all  
434 frequencies with significant amplitudes in the light curves, and dipole mode period spacing  
435 patterns are shown graphically for all 26 SPB stars in Supplementary Figures 1 to 26.  
436 Overall, we treat 388 g modes in the 26 stars, with mode frequencies ranging from 0.3525 to  
437  $3.4385 \text{ d}^{-1}$  and amplitudes ranging from 0.0022 to 14 parts-per-thousand (ppt). The errors  
438 of the period spacings used in this work are based on the frequency errors derived from  
439 least-squares harmonic fits to the light curves at each stage of the prewhitening. These  
440 formal errors range up to  $\sim 50$  seconds, which are much smaller than the uncertainties  
441 of the theoretical predictions for g-mode period spacings based on present-day stellar  
442 models<sup>26</sup>. The near-core rotational frequency of the stars was determined from the slope  
443 of the period spacing patterns<sup>24</sup>.

444 Asteroseismic modelling was so far done for only four *Kepler* SPB stars: KIC 10526294<sup>43</sup>,  
445 KIC 7760689<sup>30</sup>, KIC 3240411<sup>31</sup>, and KIC 8324482<sup>39</sup>, where the latter star is a very slow  
446 rotator with a high level of envelope mixing, interpreted in terms of shear mixing due to  
447 differential rotation by the authors. KIC 10526294, on the other hand, is also an ultra-  
448 slow rotator<sup>44</sup> with modest envelope mixing. These four previous applications considered  
449 constant envelope mixing and **hardly** assessed the quality of the input physics of stellar  
450 models, as this requires a systematic homogeneous modelling application to an ensemble  
451 of SPB stars. Here, we provide such an application based on a statistical approach<sup>26</sup>.  
452 While this may lead to less precise results compared to a grid-based approach dedicated  
453 to a single star, it offers a coherent framework, allowing to assess the quality of various  
454 theories of stellar evolution<sup>45</sup>. For the current application, we specifically evaluate the  
455 quality of stellar models with eight different internal mixing profiles (cf. Figure 3).

## 456 **Fundamental parameters of the sample stars**

457 Aside from the *Kepler* light curves (Supplementary Figures 1 to 26), high-resolution  
458 spectra for the 15 brightest SPB stars were assembled with the HERMES spectrograph

459 mounted on the 1.2-m Mercator telescope<sup>46</sup> and with the ISIS spectrograph on the William  
 460 Herschel Telescope, both located on La Palma, Spain. Three stars are known to be bina-  
 461 ries with an orbital period much longer than the periods of the  $g$  modes<sup>47</sup>. We performed  
 462 a standard reduction of the data, following earlier analyses for some of the stars<sup>42</sup>. After  
 463 manually normalizing the spectra via spline fitting, we determined the effective tem-  
 464 perature ( $T_{\text{eff}}$ ), gravity ( $\log g$ ), metallicity ( $[M/H]$ ), projected rotation velocity ( $v \sin i$ ),  
 465 and individual abundances using the publicly available Grid Search in Stellar Paramete-  
 466 ters spectral synthesis code based on synthetic spectra resulting from LTE-based model  
 467 atmospheres<sup>48</sup>. The results for the global stellar parameters are shown in blue in the  
 468 histograms in Supplementary Figure 31, where we also included the luminosity of the 26  
 469 stars based on Gaia DR2 astrometry<sup>35</sup>. For the 11 SPB stars without high-resolution  
 470 spectroscopy, we assembled lower-precision estimates of  $T_{\text{eff}}$ ,  $\log g$ , and  $[M/H]$  from the  
 471 literature. For some of the histograms in Supplementary Figure 31, we also show the  
 472 distribution of the sample of 37 OB-type stars with available nitrogen abundances and  
 473 rotation frequencies<sup>49</sup>.

474 The asteroseismic surface nitrogen abundance covered by the two grids with shear  
 475 envelope mixing is shown graphically in Supplementary Figure 32. The asteroseismic  
 476 predictions indicated on the plot are those resulting from the best  $\theta$  for that particular  
 477 grid obtained for the 26 SPB stars. The spectroscopic measurements available for 15 SPB  
 478 stars are in good agreement with the asteroseismic ones, reaching the  $1\sigma$  level for 11 of  
 479 the 15 SPB star and the  $2\sigma$  level for the four additional ones.

## 480 **Grids of evolutionary models and their pulsation modes**

481 The asteroseismic modelling of the ensemble of SPB stars relies on eight grids of non-  
 482 rotating stellar models constructed using the MESA code, adopting the MESA Equation  
 483 of State<sup>50</sup>. We rely on 1-D spherically symmetric equilibrium models, where the effects of  
 484 rotation, magnetism, waves, radiative levitation, etc., are only taken into account at the  
 485 level of the element transport via Eq. (1) by means of an unknown local time-independent  
 486 diffusion coefficient  $D_{\text{mix}}(r)$ <sup>45</sup>. This approach does not include angular momentum trans-

487 port, since its theory remains uncalibrated for the phase of hydrogen fusion according  
 488 to asteroseismic measurements<sup>45,51</sup>. For this reason, we do not include such transport  
 489 but rather estimate the internal rotation frequency at the evolutionary stage of each star  
 490 in the sample. We use the Ledoux criterion for convection and include the predictive  
 491 premixing scheme to compute the convective core boundary<sup>50</sup>.

492 OP opacity tables<sup>52</sup> applied to the initial chemical mixture of nearby B-type stars<sup>53</sup>  
 493 were used<sup>43</sup>. The models were evolved starting from the Hayashi track to the end of  
 494 the hydrogen fusion in the core, ensuring time steps below 0.001% of the nuclear time  
 495 scale. Once the zero-age-main-sequence (ZAMS) is reached the mesh refinement of the  
 496 models near the core boundary region is increased, and the Vink hot wind scheme<sup>54</sup> is  
 497 switched on assuming a wind scaling factor of 0.3<sup>55</sup>. The atmospheric table option in  
 498 MESA is applied as the outer boundary conditions for the stellar models, and the full  
 499 pp-chain and CNO cycle networks are included in the nuclear network. For a given initial  
 500  $Z$ , the initial hydrogen  $X_{\text{ini}}$  and helium  $Y_{\text{ini}}$  mass fractions are adjusted such that the  
 501 ratio  $X_{\text{ini}}/Y_{\text{ini}} = X_{\star}/Y_{\star}$  is constant across all stellar models, where  $X_{\star}$  and  $Y_{\star}$  correspond  
 502 to the Galactic standard values for B stars in the solar neighbourhood<sup>53</sup>.

503 The only difference in the input physics between the eight grids is the internal chemical  
 504 mixing profile described by the local diffusion coefficient  $D_{\text{mix}}(r)$ . The eight choices for  
 505 the profiles of the diffusion coefficients are shown schematically in Figure 3. For all eight  
 506 model grids  $D_{\text{conv}}(r)$  is based on the mixing-length theory of convection<sup>56</sup>. Two choices  
 507 for the mixing profile in the core boundary layer,  $D_{\text{cbl}}(r)$ , were considered. A first choice  
 508 for  $D_{\text{cbl}}(r)$  is an exponentially decaying function described by the parameter  $\alpha_{\text{cbl}} = f_{\text{ov}}$   
 509 and representing diffusive convective overshoot mixing<sup>27</sup> in a zone with the radiative  
 510 temperature gradient (grids denoted as  $\psi_1, \dots, \psi_4$  in Figure 3). A second choice is a step  
 511 function based on convective penetration<sup>12</sup> leading to full instantaneous mixing over a  
 512 distance expressed by the parameter  $\alpha_{\text{cbl}} = \alpha_{\text{pen}}$ . In this case, the temperature gradient  
 513 in the boundary layer is taken to be the adiabatic one (grids  $\psi_5, \dots, \psi_8$  in Figure 3).  
 514 Each of these two  $D_{\text{cbl}}(r)$  profiles is stitched to four options for  $D_{\text{env}}(r)$  at the mixing  
 515 level determined by the free parameter  $D_{\text{env},0}$ . The four options for the envelope mixing

516 represent 1) a constant profile<sup>43</sup>, 2) a profile due to internal gravity waves<sup>28</sup>, 3) a profile  
 517 typical of vertical shear due to various types of instabilities<sup>29</sup>, and 4) a profile due to  
 518 meridional circulation in the presence of vertical shear<sup>4</sup>.

519 For each of the eight grids, six free parameters are considered. These are the initial  
 520 mass  $M_{\text{ini}} \in [2.75, 10] M_{\odot}$ , the initial metal mass fraction  $Z \in [0.003, 0.04]$ , where the  
 521 range is chosen based on the observed metallicities, the ratio of the current to initial hy-  
 522 drogen mass fraction in the stellar core  $X_c/X_{\text{ini}} \in [0.99, 0.02]$ , the extent of the convective  
 523 boundary mixing region ( $f_{\text{ov}} \in [0.005, 0.04]$  and  $\alpha_{\text{pen}} \in [0.05, 0.40]$ ), the level of enve-  
 524 lope mixing at the position where the transition from convective core boundary mixing  
 525 to envelope mixing happens ( $D_{\text{env},0} \in [10, 10^6] \text{ cm}^2 \text{ s}^{-1}$ ), and the rotational frequency of  
 526 the star with respect to the critical rotation rate  $\Omega_{\text{rot}} = [0, 0.7] \Omega_{\text{crit}}$ . The dipole g-mode  
 527 frequencies for each of the models in the grids were computed taking into account the  
 528 Coriolis acceleration in the Traditional Approximation of Rotation (TAR), which offers a  
 529 valid approximation for the range of rotation rates considered here. Indeed, it was shown  
 530 that the TAR based on 1-D models performs well for dipole prograde and zonal modes  
 531 for stars rotating up to  $\sim 70\%$  of their critical break-up velocity by comparing the  
 532 computed frequencies with those obtained from 2-D models deformed by the centrifugal  
 533 acceleration<sup>57</sup>. The pulsation frequencies using the TAR were computed with the GYRE  
 534 pulsation code<sup>58</sup> for all radial orders in the range  $|n| \in [1, 80]$  and constitute the theoretical  
 535 input for the modelling procedure.

536 The sampling in parameter space for  $(M_{\text{ini}}, Z, f_{\text{ov}}, D_{\text{env},0})$  and  $(M_{\text{ini}}, Z, \alpha_{\text{pen}}, D_{\text{env},0})$   
 537 was done using a quasi-random sampling based on Sobol numbers<sup>59</sup>. Sampling these  
 538 **two sets of four** parameter ranges 2500 times is sufficient for determining the statistical  
 539 models adopted in the modelling procedure. **Supplementary Figure 33 illustrates what**  
 540 **this 2500 grid point quasi-random sampling looks like for the  $(M_{\text{ini}}, Z, f_{\text{ov}}, D_{\text{env},0})$  set of**  
 541 **parameters in comparison to a linear grid sampling.** For each of the 2500 initial starting  
 542 parameters, stellar models are computed and stored for  $X_c/X_{\text{ini}} = 0.99, 0.95$  and for each  
 543 0.05 decrease in  $X_c/X_{\text{ini}}$  down to 0.20. Below this value, we compute the stellar models in  
 544 steps of 0.02 in order to account for the increasing occurrence of avoided crossings among

545 the frequencies<sup>45</sup>. The last stellar model on the track has  $X_c/X_{\text{ini}} = 0.02$ . Each of the eight  
546 grids have 65000 equilibrium models upon which we base the asteroseismic modelling. For  
547 each equilibrium model, we compute the dipole gravity modes in the TAR for five values  
548 of the rotational frequency  $\Omega_{\text{rot}} = [0, 0.1, 0.3, 0.5, 0.7] \Omega_{\text{crit}}$ , resulting in a total of 325000  
549 different combinations of  $\theta$  for each of the  $\psi_1, \dots, \psi_8$  grids. **These eight grids are used**  
550 **to calculate predictions of period spacing values and statistical approximations thereof as**  
551 **described in detail in the following section.**

## 552 Asteroseismic modelling per individual star and per grid

553 The four observables  $T_{\text{eff}}$ ,  $\log g$ ,  $[M/H]$ , and  $\log(L/L_{\odot})$  were used to limit the range  
554 of evolution models considered for each star. We adopted  $2\sigma$  errors to ensure a 95%  
555 probability that the star falls into the grid of models. The range in  $\Omega_{\text{rot}}$  to consider  
556 for the modelling is determined based on the observed rotational frequency range de-  
557 rived from the slope of the period spacing patterns<sup>24</sup> in Supplementary Figures 1 to 26.  
558 Statistical computations<sup>26</sup> are done to approximate the pulsation mode period spacings  
559 for each star for an additional 100000 quasi-randomly sampled grid points in the 6-D  
560 parameter space inside the observed error boxes. Per grid, these statistical models are  
561 built from the original 325000 equilibrium models. Period spacing values  $\Delta P_{\ell,m,n}$  are  
562 then predicted based on the varied parameters  $\theta = (M_{\text{ini}}, Z, X_c/X_{\text{ini}}, f_{\text{ov}}, D_{\text{env},0}, \Omega_{\text{rot}})$  or  
563  $\theta = (M_{\text{ini}}, Z, X_c/X_{\text{ini}}, \alpha_{\text{pen}}, D_{\text{env},0}, \Omega_{\text{rot}})$ .

564 Following hare-and-hound tests, the asteroseismic modelling is done from mode period  
565 spacing values, because this diagnostic reveals the best performance among the three  
566 tested cases of using 1) mode frequencies, 2) mode periods, and 3) mode period spacings.  
567 The observed period spacing values  $\Delta P_{1,m,n}$  are least prone to systematic uncertainties  
568 due to limitations in the input physics of the equilibrium models. The statistical models  
569 to predict the period spacing patterns are based upon a multivariate regression model<sup>26</sup>,  
570 written as:

$$Y_{ji} = \mathbf{x}_{ji}^{\top} \boldsymbol{\beta}_j, \quad (2)$$

571 where  $Y_{ji}$  corresponds to the observable  $i$  of the grid point  $j$  (e.g.  $\Delta P_{1,1,80,j}$ ), while  $\mathbf{x}_{ji}$  are  
572 functions of  $\boldsymbol{\theta}$  based on the principle of fractional polynomials<sup>26</sup>, and  $\boldsymbol{\beta}_j$  are the regression  
573 coefficients. For each observable  $Y_{ji}$ , the optimal number of regression coefficients is  
574 determined from statistical model selection based on the Bayesian Information Criterion  
575 applied to the nested regression models<sup>60</sup>. The typical number of regression coefficients  
576 to approximate each period spacing prediction ranges from 18 to 30, depending on the  
577 grid considered.

578 Theoretical period spacing patterns ( $\Delta P^{\text{theo}}$ ) covering ranges in radial orders from  $n \in$   
579  $[1, 80]$  were matched to observed values ( $\Delta P^{\text{obs}}$ ) in three different ways: 1) the theoretical  
580 patterns are built starting from the lowest mode period in the observed patterns, matching  
581 it by finding the  $\Delta P^{\text{theo}}$  value that results in the smallest difference in any given grid point  
582 and assigning the rest of the theoretical  $\Delta P$  values such that they are consecutive in radial  
583 order; 2) the matching of the theoretical patterns is done from the two period spacings  
584 resulting from the observed mode with the highest amplitude in the periodograms and  
585 enforcing consecutive radial orders; 3) among the differences between the  $\Delta P^{\text{obs}}$  and all  
586 of the  $\Delta P^{\text{theo}}$  in a given grid point, we search those delivering the longest matching  
587 sequence in consecutive radial orders and assign the rest of the  $\Delta P^{\text{theo}}$  values according  
588 to this sequence by enforcing consecutive radial orders for the remaining  $\Delta P^{\text{theo}}$ . For each  
589 of the three ways of constructing  $\Delta P^{\text{obs}}$  and  $\Delta P^{\text{theo}}$ , we search for the best fit between  
590 the observables and theoretical predictions by applying the statistical method based on  
591 the Mahalanobis distance (MD) as the merit function<sup>26</sup>. The details are omitted here  
592 for brevity. This merit function represents a more general distance compared to the  
593 Euclidean distance, which is a special case and corresponds to a  $\chi^2$  based merit function.  
594 The Mahalanobis distance optimization takes the form

$$\text{MD} = \underset{\boldsymbol{\theta}}{\text{argmin}} \{ (\Delta P^{\text{theo}}(\boldsymbol{\theta}) - \Delta P^{\text{obs}})^{\top} (V + \Sigma)^{-1} (\Delta P^{\text{theo}}(\boldsymbol{\theta}) - \Delta P^{\text{obs}}) \}, \quad (3)$$

595 where the notation  $X^{\top}$  stands for the transpose of  $X$ ,  $V$  is the variance-covariance matrix  
596 of the vector  $\Delta P^{\text{theo}}(\boldsymbol{\theta})$  for each of the grids  $\boldsymbol{\psi}_1, \dots, \boldsymbol{\psi}_8$  and  $\Sigma$  is the matrix with diagonal  
597 elements given by the observational errors of the  $i = 1, \dots, N$  measured period spacings.

598 The values of  $\Delta P^{\text{theo}}(\boldsymbol{\theta})$  are taken from the statistical grids of stellar model predictions  
 599 constructed for each of the eight  $\boldsymbol{\psi}$  values. The Mahalanobis distance defined by Eq. (3)  
 600 takes full account of the fact that theoretical uncertainties in the predictions  $\Delta P^{\text{theo}}$  are  
 601 typically two orders of magnitude larger than the observational uncertainties of  $\Delta P^{\text{obs}}$   
 602 measured from 4-year *Kepler* data<sup>26</sup> and includes the overall correlated nature of the  
 603 parameters  $\boldsymbol{\theta}$  and the observables  $\Delta P^{\text{theo}}$ . The stability of the solution for MD resulting  
 604 from Eq. (3) is determined by the eigenvalues of the matrix  $V + \Sigma$ , which captures the  
 605 combined theoretical and measurement covariance structure of the quantities used in the  
 606 modelling. This stability is set by the so-called condition number of this matrix. We  
 607 retain the solution of Eq. (3) for that problem set among the three ways of constructing  
 608 the theoretical period spacing patterns delivering the smallest condition number.

609 The solution for MD is computed several times for each star and for each grid  $\boldsymbol{\psi}_1, \dots, \boldsymbol{\psi}_8$ ,  
 610 relying on different combinations of  $T_{\text{eff}}$ ,  $\log g$ , and  $\log(L/L_{\odot})$  as error box to compute  
 611 the statistical regression models for  $\Delta P^{\text{theo}}(\boldsymbol{\theta})$ . That is because the measurement quality  
 612 of these classical observables is different per star. Moreover, the character of the period  
 613 spacing patterns also differs strongly from star to star. Some stars deliver more than  
 614 one option to construct the observational patterns<sup>31</sup>. For all these various solutions from  
 615 Eq. (3), we kept the one relying on the variance-covariance matrix with the lowest con-  
 616 dition number. In practice, the condition numbers encountered for each of the 26 SPB  
 617 stars range over 26 - 7000.

618 The retained solutions to Eq. (3) were then subjected to statistical model selection  
 619 based on the Akaike Information Criterion corrected for small numbers<sup>60</sup>, AICc, given  
 620 that the number of components in the observed patterns for the 26 SPB stars range from  
 621 7 to 34 (cf. Supplementary Figures 1 to 26). The overall best solution for  $\boldsymbol{\theta}$  per star and  
 622 per grid  $\boldsymbol{\psi}_1, \dots, \boldsymbol{\psi}_8$  is then selected from the lowest AICc combined with visual inspection  
 623 among all the computed cases for the MD and AICc values. A fully automated process  
 624 is sub-optimal because the AICc, as well as any alternative selection criterion, depends  
 625 on outlier behaviour<sup>60</sup>. For our application to period spacing patterns, this implies that  
 626 the AICc can pick a solution with a low AICc value due to a particular trapped mode,

627 which may act as an outlier in the pattern. The diversity in deviations from a constant  
628 period spacing is large, as illustrated in Supplementary Figures 1 to 26, such that visual  
629 inspection is warranted. The outcome of the asteroseismic modelling for the 26 SPB stars  
630 is listed in Supplementary Tables 1 and 2, and shown graphically in the bottom panels of  
631 Supplementary Figures 1 to 26.

632 For the global stellar  $\theta$  components, i.e., the mass, metallicity, evolutionary stage,  
633 and rotation frequency, it is meaningful to compute an averaged value weighted accord-  
634 ing to MD across the eight grids. The standard deviation with respect to this average  
635 provides an estimate of the systematic uncertainty for these parameters due to the un-  
636 known internal mixing physics. The outcome is provided in Supplementary Table 2 and  
637 shows that the four  $\theta$  components agree with the averaged value across the eight grids  
638 to within the standard deviation for 19 of the 26 SPB stars. Precision estimation of  $\theta$   
639 per grid is a notoriously difficult issue because the components of the parameter vector  
640 are strongly correlated for g-mode asteroseismology in stars with a convective core<sup>43</sup>. It  
641 is not meaningful to assess the precision of each  $\theta$  ignoring this correlation. Rather, one  
642 has to compute 6-D uncertainty regions. We handle this by a Monte Carlo approach, by  
643 perturbing the regression coefficients  $\beta$  in Eq. (2) 100 times and recomputing the MD and  
644  $\theta$  solution accordingly. The outcome is shown graphically by means of projected error  
645 ranges in Supplementary Figures 1 to 26, but we stress that these projections onto a single  
646  $\theta$  component axis should not be interpreted as being independent error estimates in 1-D.

## 647 **Data availability**

648 The data that support the plots within this paper and other findings of this study are  
649 available from the corresponding author upon reasonable request.

## 650 **Code availability**

651 The iterative pre-whitening code is freely available and documented at  
652 <https://github.com/IvS-KULeuven/IvSPythonRepository>. The stellar evolution code, MESA,

653 is freely available and documented at <http://mesa.sourceforge.net/>. The stellar pulsa-  
654 tion code, GYRE, is freely available and documented at  
655 <https://bitbucket.org/~rhdtownsend/gyre/wiki/Home>.

## 656 Acknowledgements

657 The authors are grateful to the MESA and GYRE code developers for their efforts, public  
658 dissemination, and training initiatives to make their software so accessible to the world-  
659 wide astrophysics community. The authors thank Dr. Sylvia Ekström of the Geneva  
660 Observatory for having provided mixing profiles from Georgy et al. (2013) in electronic  
661 format. We acknowledge the work of the teams behind the NASA *Kepler* and ESA Gaia  
662 space missions. This work is based on observations with the HERMES spectrograph at  
663 the Mercator Telescope which is operated at La Palma/Spain by the Flemish Commu-  
664 nity. This research has made use of the SIMBAD database, operated at CDS, Strasbourg,  
665 France and of NASA’s Astrophysics Data System. The research leading to these results  
666 has received funding from the European Research Council (ERC) under the European  
667 Union’s Horizon 2020 research and innovation programme (grant agreement N°670519:  
668 MAMSIE), from the National Science Foundation (Grant No. NSF PHY-1748958), from  
669 the KU Leuven Research Council (grant C16/18/005: PARADISE), and from the Re-  
670 search Foundation Flanders (FWO) by means of PhD Fellowships to M.M. and S.G.  
671 under contract N°11F7120N and N°11E5620N, and a senior post-doctoral fellowship to  
672 D.M.B. with grant agreement N°1286521N. Funding for the *Kepler* Mission was provided  
673 by NASA’s Science Mission Directorate. Gaia data are being processed by the Gaia Data  
674 Processing and Analysis Consortium (DPAC); funding for the DPAC is provided by na-  
675 tional institutions, in particular the institutions participating in the Gaia MultiLateral  
676 Agreement (MLA).

## 677 **Author contributions**

678 M.G.P performed frequency analysis and mode identification, wrote code to include mix-  
679 ing profiles in MESA, computed asteroseismic observables, implemented and applied the  
680 modelling procedures, interpreted the results, and wrote part of the text. C.A. defined  
681 the research, developed the modelling procedure, interpreted the results, and wrote part  
682 of the text. P.I.P constructed light curves from the raw *Kepler* data and discovered the  
683 targets to be new SPB stars. M.M. wrote code to include mixing profiles in MESA and  
684 assessed the capacity of observables used for the modelling. S.G. determined abundances  
685 from spectroscopy. T.M.R. computed and provided envelope mixing profiles due to in-  
686 ternal gravity waves. G.M. provided advice on the parameter estimation and statistical  
687 model selection and performed the cluster analysis. S.B., S.G., and D.M.B. contributed  
688 to the frequency analysis and interpretation. All authors contributed to the discussions  
689 and have read and iterated upon the text of the final manuscript.

## 690 **Competing interests**

691 The authors declare no competing interests.

## 692 **Materials & Correspondence**

693 Correspondence and requests for materials should be addressed to the corresponding au-  
694 thor May Gade Pedersen (mgpedersen@kitp.ucsb.edu).

## 695 **Additional information**

696 **Supplementary Information** is available for this paper.

697 **Correspondence and requests for materials** should be addressed to M.G.P.

698 **Reprints and permissions information** is available at [www.nature.com/reprints](http://www.nature.com/reprints)